AAAS
Energy Material Advances
Volume 2021, Article ID 9895403, 14 pages
https://doi.org/10.34133/2021/9895403

Energy Material Advances
A SCIENCE PARTNER JOURNAL

Research Article

Ion Coordination and Transport in Magnesium Polymer Electrolytes Based on Polyester-co-Polycarbonate

Bumjun Park,[1] **Rassmus Andersson**,[2] **Sarah G. Pate**,[1] **Jiacheng Liu**,[1] **Casey P. O'Brien**,[1] **Guiomar Hernández**,[2] **Jonas Mindemark**,[2] **and Jennifer L. Schaefer**[1]

[1]*Department of Chemical and Biomolecular Engineering, University of Notre Dame, Notre Dame, IN 46556, USA*
[2]*Department of Chemistry-Ångström Laboratory, Uppsala University, Box 538, SE-751 21 Uppsala, Sweden*

Correspondence should be addressed to Jennifer L. Schaefer; jennifer.l.schaefer.43@nd.edu

Received 24 June 2021; Accepted 20 August 2021; Published 15 September 2021

Magnesium-ion-conducting solid polymer electrolytes have been studied for rechargeable Mg metal batteries, one of the beyond-Li-ion systems. In this paper, magnesium polymer electrolytes with magnesium bis(trifluoromethane)sulfonimide ($Mg(TFSI)_2$) salt in poly(ε-caprolactone-*co*-trimethylene carbonate) (PCL-PTMC) were investigated and compared with the poly(ethylene oxide) (PEO) analogs. Both thermal properties and vibrational spectroscopy indicated that the total ion conduction in the PEO electrolytes was dominated by the anion conduction due to strong polymer coordination with fully dissociated Mg^{2+}. On the other hand, in PCL-PTMC electrolytes, there is relatively weaker polymer–cation coordination and increased anion–cation coordination. Sporadic Mg- and F-rich particles were observed on the Cu electrodes after polarization tests in Cu|Mg cells with PCL-PTMC electrolyte, suggesting that Mg was conducted in the ion complex form (Mg_xTFSI_y) to the copper working electrode to be reduced which resulted in anion decomposition. However, the Mg metal deposition/stripping was not favorable with either $Mg(TFSI)_2$ in PCL-PTMC or $Mg(TFSI)_2$ in PEO, which inhibited quantitative analysis of magnesium conduction. A remaining challenge is thus to accurately assess transport numbers in these systems.

1. Introduction

Energy storage devices need to be improved for further electrification of transportation and energy storage systems for renewable energy sources. To meet these demands, beyond-Li-ion battery systems have gained attention. Among the beyond-Li-ion battery systems, rechargeable Mg metal batteries are an attractive system due to the abundance of magnesium and the high volumetric capacity of Mg metal anodes. Rechargeable Mg metal batteries have been researched for 30 years with nonaqueous electrolytes including Grignard reagents, hexamethyldisilazanes, borohydrides, and halide-based salt complexes in ether-based organic solvents [1–6]. Though those early-stage electrolytes displayed reversible cycling on Mg metal anodes, the poor compatibility with the other cell components hinders their commercialization due to their low oxidative stability and highly reactive/corrosive nature [7]. Recent studies on simple liquid electrolytes based on carborane- and borate-based salts are promising, with the alleviation of the reactivity issues [8–11]. Yet they still include ether-based solvents, which might not be suitable for some applications due to volatility, flammability, and possible leakage.

Solid polymer electrolytes (SPEs) are potentially advantageous due to higher thermal, mechanical, and electrochemical stability compared with liquid electrolytes as well as lower cost and density relative to inorganic solid-state electrolytes [12, 13]. While lithium cation- (Li^+-) conducting SPEs have been widely researched [13–15], reports on successful magnesium cation- (Mg^{2+}-) conducting SPEs for magnesium metal batteries are relatively limited [12, 16–18]. Magnesium metal is easily passivated by common aprotic organic liquid solvents and common anions [19–22]. In addition, the high charge density of Mg^{2+} results in significant coordination with anions as well as polar functional groups of polymer hosts, slowing down the polymer host segmental motion [12, 13]. The total ion conduction in magnesium polymer electrolytes is often dominated by the anion conduction

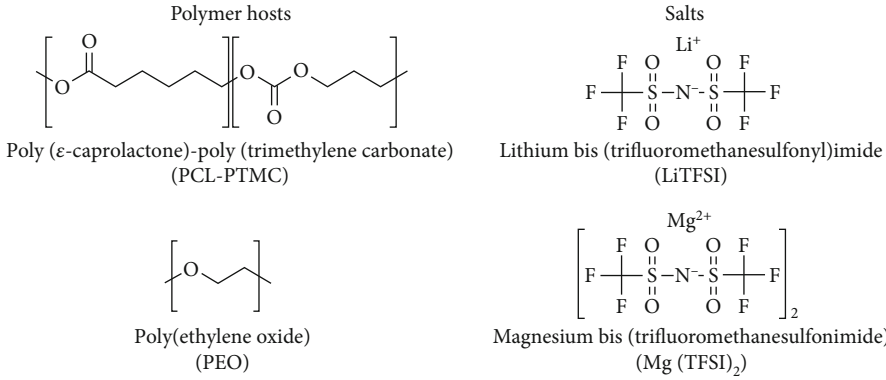

Figure 1: Chemical structures of polymer hosts and salts.

with very limited magnesium conduction due to the strong coordination of Mg^{2+} with the polar functional groups of polymer hosts [16, 17]. Thus, it is required to characterize magnesium conduction separated from the total ion conduction.

It has been reported that poly(trimethylene carbonate) (PTMC) allows for higher lithium (~0.80) and sodium (~0.48) cation transference number at 60°C relative to analogous poly(ethylene oxide) (PEO) electrolytes (0.1–0.2) due to the weaker interaction between the metal ions and the polymer hosts, even though they showed lower total ionic conductivity (~10^{-7} S cm^{-1}) than PEO analogs (~10^{-4} S cm^{-1}) [23–26]. The ionic conductivity was improved by introduction of a copolymer host poly(ε-caprolactone-*co*-trimethylene carbonate) (PCL-PTMC) (~10^{-4} S cm^{-1}), where the caprolactone (CL) units increased the overall chain flexibility and optimization was achieved at CL : TMC = 80 : 20 in molar ratio [27]. Even though the lithium transference number was somewhat compromised when compared to PTMC (0.66 vs. 0.80 at 60°C), it is still much higher than for PEO with comparable total ion conduction, which results in higher net lithium conduction [27].

Here, we report on magnesium SPEs based on magnesium bis(trifluoromethane)sulfonimide ($Mg(TFSI)_2$) salt in PCL-PTMC and compare with the PEO analogs. While $Mg(TFSI)_2$-containing magnesium electrolytes are often problematic due to Mg metal surface passivation, this phenomenon is known to be impacted by TFSI coordination state and could in the future be avoided by use of an artificial magnesium-conducting solid electrolyte interphase [28–31]. Hence, it is worthwhile to understand ion speciation and transport in polymer electrolytes based on this simple salt. It was observed that PCL-PTMC readily went from slightly crystalline to fully amorphous with the addition of magnesium salt. The population of $TFSI^-$ and polar polymer moieties in different coordination states were studied via Raman and FT-IR [25, 32, 33]. Investigation of ion conduction mechanisms and Mg conduction/deposition indicated that the ion conduction likely occurred in the form of the ion complex (such as $[MgTFSI]^+$ or $[Mg_2TFSI_3]^+$) rather than free Mg^{2+}.

2. Materials and Methods

2.1. Materials. Lithium bis(trifluoromethane)sulfonimide (LiTFSI, TCI) salt was dried under vacuum for 24 h at 120°C. $Mg(TFSI)_2$ (Solvionic) salt was dried under vacuum for 24 h at 200°C. Poly(ethylene oxide) (PEO, Sigma, MW = 100,000 g mol^{-1}) was dried under vacuum at room temperature for 3 days prior to use. The drying of LiTFSI, $Mg(TFSI)_2$, and PEO was conducted in an argon-filled glove box. Acetonitrile (anhydrous, Sigma) was used as received. Poly(ε-caprolactone-*co*-trimethylene carbonate) (PCL-PTMC, 80 : 20 molar ratio, MW = 246, 000 – 338,000 g mol^{-1}) was synthesized by following the previously reported methods [23, 27]. The molecular structures of each of the polymers and salts are shown in Figure 1.

2.2. Polymer Electrolyte Preparation. Free-standing polymer electrolyte films were prepared via solution casting in an argon-filled glove box. The detailed procedure was reported previously [27]. In brief, $Mg(TFSI)_2$ and PCL-PTMC in various ratios were stirred in acetonitrile for 8 h. The solution was then cast in a Teflon beaker at room temperature for 24 h to evaporate the bulk solvent and then further dried at room temperature under vacuum for 24 h and at 60°C for 48 h, to prepare polymer electrolyte films (thickness~100 μm) with 8–36 wt.% $Mg(TFSI)_2$ in PCL-PTMC. Polymer electrolyte films of 8–36 wt.% $Mg(TFSI)_2$ in PEO and 20–36 wt.% LiTFSI in PCL-PTMC were prepared with the same procedure. The molar ratios of metals to the coordinating groups in the polymers are listed in Tables 1–3.

2.3. Differential Scanning Calorimetry (DSC). Samples (3–7 mg) were hermetically sealed in aluminum pans in an argon-filled glove box. The samples underwent a heating-cooling-heating cycle from -80°C to 130°C at a scan rate of 10°C min^{-1} under nitrogen purge at 50 mL min^{-1}. The glass transition temperatures reported were obtained from the second heating scan. DSC experiments were performed on a DSC Q2000 (TA Instruments).

2.4. Ionic Conductivity and Dielectric Analysis. Sample films were punched and sandwiched between two brass electrodes along with glass fiber spacers to maintain the inter-electrode distance as 53 μm. The conductivity cell was assembled and then aged at 120°C for 2 h to improve the contact with the electrodes, cooled to room temperature, and aged for another 24 h (to stabilize the polymer phase

Table 1: Molar ratio of polar functional groups to Mg^{2+} and positive charge ($[1/2\ Mg]^+$) in $Mg(TFSI)_2$ in PCL-PTMC electrolytes investigated.

Salt concentration (wt.%) $Mg(TFSI)_2$	Ratio of functional groups			
	$CL:Mg^{2+}$	$TMC:Mg^{2+}$	$[CL+TMC]:Mg^{2+}$	$[CL+TMC]:[1/2\ Mg]^+$
8	47.1	13.2	60.3	120.6
12	30.0	8.4	38.4	76.9
16	21.5	6.0	27.5	55.0
20	16.4	4.6	21.0	41.9
28	10.5	2.9	13.5	27.0
36	7.3	2.0	9.3	18.6

Table 2: Molar ratio of coordinating groups to Mg^{2+} and positive charge ($[1/2\ Mg]^+$) in $Mg(TFSI)_2$ in PEO electrolytes investigated.

Salt concentration (wt.%) $Mg(TFSI)_2$	Ratio of functional groups	
	$EO:Mg^{2+}$	$EO:[1/2\ Mg]^+$
8	152.6	305.2
12	97.3	194.6
16	69.7	139.3
20	53.1	106.2
28	34.1	68.3
36	23.6	47.2

Table 3: Molar ratio of coordinating groups to Li^+ in LiTFSI in PCL-PTMC electrolyte investigated.

Salt concentration (wt.%) LiTFSI	Ratio of functional groups		
	$CL:Li^+$	$TMC:Li^+$	$[CL+TMC]:Li^+$
20	8.0	2.2	10.3
28	5.2	1.4	6.6
36	3.6	1.0	4.6

and to allow for possible crystallization). Ionic conductivity and permittivity of samples were measured on a broadband dielectric spectrometer with an Alpha A analyzer and Quatro temperature control unit with a cryostat (Novocontrol Technologies, Montabaur, Germany). The measurements were conducted over a frequency range of 10^7–10^{-1} Hz with an amplitude of 0.1 V over a temperature range from -20 to 120°C in 20°C intervals. The temperature was stabilized at each point for 10 min within 0.5°C before each measurement.

2.5. Raman Spectroscopy. Samples were sealed in quartz cuvettes, followed by aging at 120°C for an hour before measurement. All sample cuvettes were prepared in an argon-filled glove box. Raman spectra were obtained using Jasco NRS-5100 with excitation laser with a wavelength of 532 nm. The signal was calibrated with a silicon wafer at a wavenumber of 520.7 cm^{-1}. Raman spectra were obtained with 5–10 scans for 1–2 min, which sums up to total scan time of around 10 min. The spectrum of the $TFSI^-$ stretching peak around 740 cm^{-1} was deconvoluted with Gaussian functions using a home-made Python program.

2.6. Fourier-Transform Infrared (FT-IR) Spectroscopy. The FT-IR spectroscopy was measured using a Tensor II FT-IR spectrometer equipped with a liquid nitrogen-cooled mercury-cadmium-telluride detector (Bruker). Each sample film was attached to an aluminum disk holder, which was sealed in an airtight cell equipped with zinc selenide viewports for optical access, in an argon-filled glove box. Data were obtained in a transmission mode with a resolution of 4 cm^{-1} and 64 scans.

2.7. Coordination Assessment by FT-IR Spectroscopy in Solution. The FT-IR spectroscopy was performed using a Bruker Vertex 70v FT-IR spectrometer with a liquid nitrogen-cooled MCT detector. The samples were prepared with a constant $Mg(TFSI)_2$ concentration of 100 mM in propionitrile as a function of the polymer concentration in the range 0 M to 2 M. The measurements of each polymer concentration were made in triplicates. In air, the samples were injected into an Omni transmission cell from Specac with calcium fluoride (CaF_2) glass windows separated by a 0.012 mm mylar spacer. The measurements were performed in transmission mode with a resolution of 1 cm^{-1} and 256 scans. The Omni transmission cell compartments were cleaned with acetone and ethanol between each sample injection and measurement. Spectra were obtained for solutions containing different ratios of coordinating oxygen to Mg^{2+} cations (n). The apparent coordination number (CN_{app}) was calculated as $CN_{app} = \chi \times n$, where χ is the ratio of the coordinated nitrile peak area to the area of the non-coordinated nitrile peak.

2.8. Electrochemical Measurements. Electrochemical polarization tests were conducted using a PARSTAT MC1000 (Princeton Applied Research) potentiostat. Two-electrode coin cells (CR2032) were assembled as follows. Sample films (28 and 36 wt.% $Mg(TFSI)_2$ in PCL-PTMC, 16 wt.% $Mg(TFSI)_2$ in PEO) were punched and sandwiched between working (Cu foil) and counter (Mg foil) electrodes (Cu|Mg cells). Coin cells with a Li foil counter electrode (Cu|Li cells) were also prepared with 28 and 36 wt.% $Mg(TFSI)_2$ in PCL-PTMC for comparison. The polarization tests were conducted at 80°C. The cells were rested for 24 h and then polarized at -0.8 V vs. Mg (Cu|Mg cells) or -0.1 V vs. Li (Cu|Li cells) for 20 hours. Electrochemical impedance spectroscopy (EIS) was conducted before and after polarization at 80°C at the same DC voltage as the polarization step, an

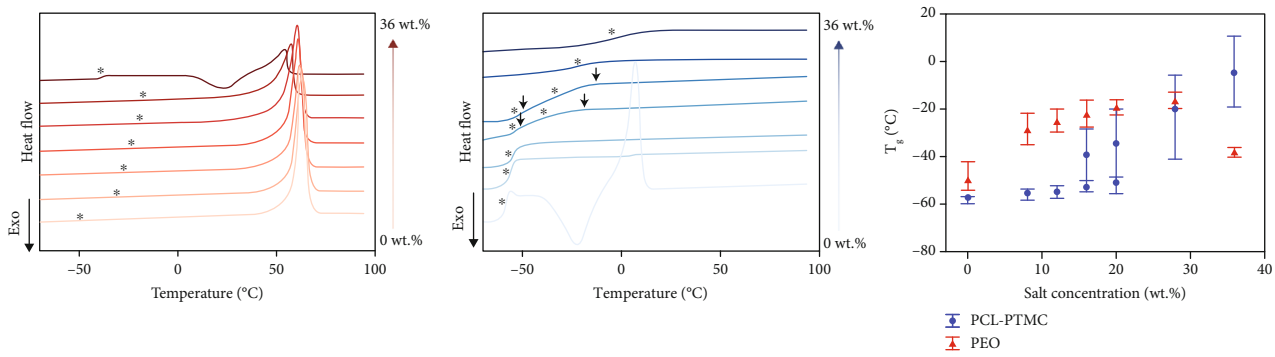

FIGURE 2: DSC scans of 0-36 wt.% $Mg(TFSI)_2$ in (a) PEO and (b) PCL-PTMC, where ∗ and ↓ are the midpoint and the bounds of the glass transitions, respectively. (c) Salt concentration vs. T_g, where error bars indicate the widths of transitions.

amplitude of 0.1 V, and the frequency range between 10^6 and 10^{-1} Hz.

2.9. Scanning Electron Microscopy (SEM) and Energy-Dispersive X-Ray Spectroscopy (EDS). The Cu electrodes after polarization were sealed in a Pelco SEM pin stub vacuum desiccator in an argon-filled glove box and then transferred to the instrument to minimize air exposure. The surface morphology of the copper (working) electrodes was obtained with a FEI Magellan 400 at an accelerating voltage of 5 kV and current of 13 pA at a working distance of 4 mm. A Bruker energy-dispersive X-ray spectrometer (EDS) was used for elemental analysis of the electrode surfaces. In order to obtain an adequate signal, the current was increased for EDS measurements.

3. Results and Discussion

3.1. Thermal Properties. Figure 2 and Figure S1 show the results of the DSC second heating scan and the differentiated heat flow curves of magnesium polymer electrolytes containing different $Mg(TFSI)_2$ concentrations in either PCL-PTMC or PEO. For nearly all samples, the glass transition temperature (T_g) increased with increased salt concentration. This is due to more physical crosslinking formed by Mg^{2+} interaction with the polar groups in the polymers, which results in less flexibility of the chain segments.

In PEO, the melting peak was observed at all concentrations of $Mg(TFSI)_2$, which indicates the existence of crystallinity. T_g increased linearly with increased salt concentration up to 28 wt.%, showing a transition width of about 10°C. T_g then decreased with an increase in concentration to 36 wt.% $Mg(TFSI)_2$ in PEO. This composition also exhibited a cold crystallization peak upon heating in lieu of crystallization upon cooling (Figure S2), likely due to slowed dynamics of the crystallization from strong interactions between Mg^{2+} and EO at this higher concentration of 36 wt.% $Mg(TFSI)_2$. Lower T_g with 36 wt.% $Mg(TFSI)_2$ in PEO can be explained by this absence of crystallinity, resulting in lower T_g as the chains are not locked in rigid crystalline structures (Table S1).

In PCL-PTMC, a cold crystallization and a melting peak were observed in the pure polymer, which disappeared with the addition of the $Mg(TFSI)_2$ salt, as expected based on the previous studies with LiTFSI salt [27]. More amorphous phase is beneficial for ion conduction via segmental motion, which is the main ion conduction mechanism for polymer electrolytes where strong coordination of polymer with cations is observed [34]. Overall, T_g was lower in PCL-PTMC than in PEO except at 36 wt.% $Mg(TFSI)_2$ (Figure 2(c)), which is an indication of weaker ion–polymer interactions in the PCL-PTMC system. Two types of glass transitions were observed over the range of salt concentration in PCL-PTMC. At low salt concentration (8, 12 wt.%), the thermal transition was observed at a low temperature (<-50°C) with a narrow width (~5°C) and the dependence of the glass transition temperature on salt concentration was weaker. At high salt concentration (28, 36 wt.%), the thermal transition was observed at a higher temperature (>-40°C) with a broad width (~30°C) and the increase of the transition temperature with salt concentration was large. At intermediate salt concentration (16, 20 wt.%), both types of glass transitions were observed. This implies that there is phase segregation, formed through spinodal decomposition, in the range of 16–20 wt.% total salt concentration. Since the narrow glass transition at lower temperature is similar to that of the pure polymer, we assume that the narrow transition may be attributed to a "lower salt concentration phase." As such, the broad glass transition at higher temperature is a transition in a "higher salt concentration phase" [35–37]. The steep increase of the "higher salt concentration phase" glass transition temperature with increased salt concentration indicates that the interactions between ions and the polymer chains were reinforced by the salt addition.

3.2. Ionic Conductivity. Figure 3 shows the total ionic conductivity (σ_{tot}), containing the contributions of both anion and cation mobilities, of PCL-PTMC-based magnesium electrolytes ($Mg(TFSI)_2$ in PCL-PTMC) and PEO-based magnesium electrolytes ($Mg(TFSI)_2$ in PEO) as a function of temperature. The PEO-based magnesium electrolytes displayed typical behavior for semicrystalline electrolytes where a drop-off in conductivity is observed at temperatures below the crystallization temperature [13]. Here, the ionic

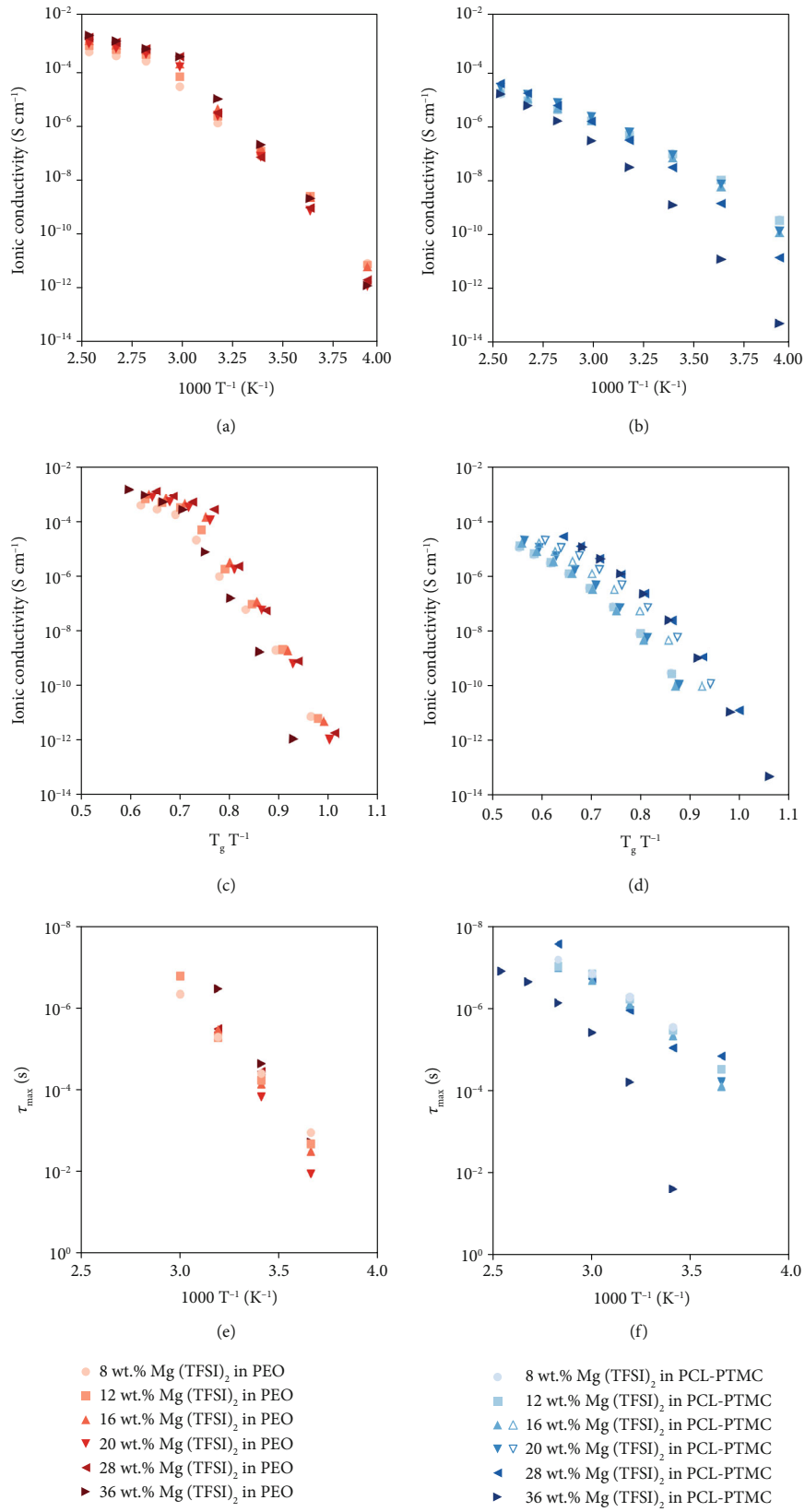

Figure 3: Ionic conductivity vs. inverse temperature (1000 T^{-1}) of $Mg(TFSI)_2$ in (a) PEO and (b) PCL-PTMC. Ionic conductivity vs. normalized temperature ($T_g\,T^{-1}$) of $Mg(TFSI)_2$ in (c) PEO and (d) PCL-PTMC, where empty markers are ionic conductivity of 16 and 20 wt.% $Mg(TFSI)_2$ in PCL-PTMC normalized by "higher salt concentration" phase transition temperature. Maximum dielectric relaxation time (τ_{max}) vs. inverse temperature (1000 T^{-1}) of $Mg(TFSI)_2$ in (e) PEO and (f) PCL-PTMC.

conductivity of the PEO-based magnesium electrolytes did not vary much as a function of salt concentration. In contrast, the PCL-PTMC-based magnesium electrolytes displayed typical behavior for amorphous electrolytes where Vogel–Tammann–Fulcher (VTF) behavior was observed, indicative of ion dynamics coupled to polymer segmental dynamics [13]. While the ionic conductivity of the PCL-PTMC-based magnesium electrolytes was almost identical up to the salt concentration of 8–28 wt.%, low ionic conductivity was observed with a more significant temperature dependence. The difference in the ionic conductivity was substantial at low temperature (decreased ~24 times from 28 wt.% (2.52×10^{-8} S cm^{-1}) to 36 wt.% (1.06×10^{-9} S cm^{-1}) $Mg(TFSI)_2$ in PCL-PTMC at 25°C). The total ionic conductivity of the PCL-PTMC-based magnesium electrolytes was higher than that of the PEO-based magnesium electrolytes at below room temperature and lower at above room temperature, although it should be noted that it is unclear from these data what the relative contribution of the magnesium cations to the conductivity is for the different polymer electrolytes.

The ionic conductivity was also plotted versus temperature normalized by the glass transition temperatures (T_g/T) (Figures 3(c) and 3(d)). Since two glass transitions were observed in the PCL-PTMC-based magnesium electrolytes at the salt concentration of 16 and 20 wt.%, the ionic conductivity was normalized by each of them, where the empty markers indicate the ionic conductivity normalized by the "higher salt concentration" transition. The ionic conductivity of the PCL-PTMC-based magnesium electrolytes was separated into two groups, showing higher ionic conductivity with the "higher salt concentration" transition (≧28 wt.%) and lower ionic conductivity with the "lower salt concentration" transition (≦12 wt.%). While normalization of the ionic conductivity of 16 and 20 wt.% by the "lower salt concentration" transition temperature results in a clear overlap with the "lower salt concentration" group, normalization with "higher salt concentration" transition temperature does not result in a clear overlap with the "higher salt concentration" group. In summary, we can say that scaling of the temperature-dependent ionic conductivity by the glass transition temperatures does not result in a master curve, which suggests that the magnitudes of the total ionic conductivity of the electrolytes are impacted by more than the segmental relaxation dynamics of the polymers; ion clustering may play a role in impacting the effective mobile ion number concentration and ion transport mechanism.

3.3. Dielectric Relaxation Analysis. Dielectric relaxation analysis was conducted to investigate the ion transport mechanism. The dielectric loss derivative (ε'_{der}) was derived from Kramers–Kronig relationship using the dielectric constant (ε') [38]:

$$\varepsilon'_{der}(\omega) = -\frac{\pi}{2}\frac{\partial \varepsilon'(\omega)}{\partial \ln \omega}. \quad (1)$$

A representative ε'_{der} vs. $\ln \omega$ plot is shown in Figure S3. Here, the curve in the high-frequency region is related to the dielectric relaxation process and the slope at mid–low-frequency region is related to the electrode polarization (EP) process. Then, the dielectric relaxation time was extracted via fitting ε'_{der} to the Havriliak–Negami (HN) equation, which gives the HN relaxation time (τ_{HN}) [38, 39]:

$$\varepsilon^* = \varepsilon_\infty + \frac{\Delta\varepsilon}{\left(1 + (i\omega\tau_{HN})^\alpha\right)^\beta} + \left(\frac{\sigma}{i\omega\varepsilon_0}\right)^n + A\omega^{-S}, \quad (2)$$

where ε_∞ is the dielectric constant at infinite high frequency, $\Delta\varepsilon$ is the dielectric relaxation strength, α and β are shape parameters, σ is the conductivity, ε_0 is the permittivity of vacuum, and n, A, and S are constants.

The maximum dielectric relaxation time (τ_{max}) was then calculated using the relation between τ_{HN} and τ_{max}:

$$\tau_{max} = \tau_{HN}\left(\sin\frac{\alpha\beta\pi}{2+2\beta}\right)^{1/\alpha}\left(\sin\frac{\alpha\pi}{2+2\beta}\right)^{-1/\alpha}. \quad (3)$$

τ_{max} was plotted vs. inverse temperature for $Mg(TFSI)_2$ in PCL-PTMC and PEO (Figures 3(e) and 3(f)). It should be noted that τ_{max} peaks for PEO electrolytes above the melting point (>60°C) were not present within the frequency measurement range of the spectrometer (maximum of 10^7 Hz). τ_{max} of $Mg(TFSI)_2$ in PEO did not change with salt concentration, which is the same trend as the ionic conductivity. τ_{max} of $Mg(TFSI)_2$ in PCL-PTMC has reduced activation energy compared with PEO and the value did not change up to 28 wt.% $Mg(TFSI)_2$, which is similar to the trend of the ionic conductivity. τ_{max} of 36 wt.% $Mg(TFSI)_2$ PCL-PTMC had VTF-type temperature dependence with much lower values than the other $Mg(TFSI)_2$ concentration. At room temperature, the segmental relaxation became 2600 times slower from 28 wt.% (9.19×10^{-6} s) to 36 wt.% (2.39×10^{-2} s) $Mg(TFSI)_2$ in PCL-PTMC. On the other hand, the ionic conductivity decreased only 24 times from 28 wt.% (2.52×10^{-8} S cm^{-1}) to 36 wt.% (1.06×10^{-9} S cm^{-1}) $Mg(TFSI)_2$ in PCL-PTMC. This implies that the ion conduction was partially decoupled from the segmental relaxation in 36 wt.% $Mg(TFSI)_2$ in PCL-PTMC, which is due to the ion conduction via a hopping mechanism through the connected "higher salt concentration" phase [40, 41].

3.4. FT-IR Spectroscopy in Propionitrile. The FT-IR spectra of $Mg(TFSI)_2$ in propionitrile were collected with addition of different concentrations of the polymers (PEO or PCL-PTMC). Depending on the strength of the coordination, the ratio of the coordination of Mg^{2+} with the nitrile relative to the polar polymer moieties will vary with addition of polymers [26]. If the fraction of Mg^{2+} coordinated to the polymer increases due to the addition of the polymer, then the fraction of Mg^{2+} coordinated to propionitrile will decrease. The relative coordination of the propionitrile population is displayed as a function of the concentration of the coordinating moieties of the polymers (Figure 4). The relative coordination for each concentration was calculated from the integrated area of the coordinated and

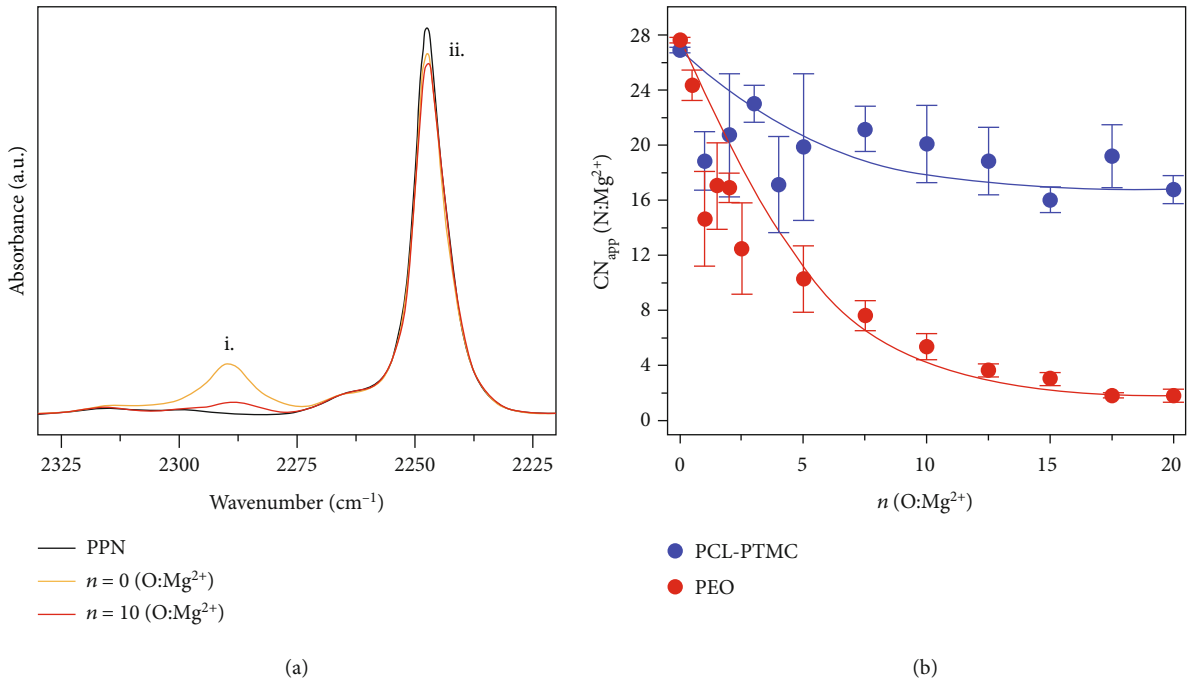

FIGURE 4: (a) FT-IR spectra of solutions of $Mg(TFSI)_2$ in propionitrile with different concentrations of PEO (given as the ratio of coordinating oxygen to Mg^{2+} cations), compared to pure propionitrile. i. indicates the nitrile:Mg^{2+} coordinating peak and ii. indicates the noncoordinating nitrile peak. (b) Apparent coordination number CN_{app} as a function of n. The values are averages of triplicate measurements with error bars representing the standard deviation of the mean. Lines represent exponential fits as described elsewhere [26].

uncoordinated nitrile peak for propionitrile together with the molar ratios of the $Mg(TFSI)_2$ and propionitrile in the solution, respectively. As PEO was added to the propionitrile solutions of $Mg(TFSI)_2$, the population of the coordinated propionitrile significantly decreased due to the strong coordination of EO groups. As PCL-PTMC was added to the propionitrile solutions of $Mg(TFSI)_2$, the population of coordinated nitrile groups decreased to a lesser extent, which implies a weaker coordination of C=O than EO with Mg^{2+}.

3.5. Vibrational Spectroscopy of SPEs. Raman spectra were collected on $Mg(TFSI)_2$ in PCL-PTMC, LiTFSI in PCL-PTMC, and $Mg(TFSI)_2$ in PEO (Figure 5, Figure S4). A strong peak around 740 cm^{-1} is related to the expansion–contraction modes of the $TFSI^-$ anion [33, 42, 43]. As the $TFSI^-$ anion interacts with cations, its stretching peak shifts to higher wavenumbers.

For $Mg(TFSI)_2$, there are three coordination states depending on the number of oxygen atoms on $TFSI^-$ that are coordinating with Mg^{2+}: 2 O (bidentate) $TFSI^-$ (752 cm^{-1}, Peak 1), 1 O (monodentate) $TFSI^-$ (746 cm^{-1}, Peak 2), and free $TFSI^-$ (739–742 cm^{-1}, Peaks 3–4) [33, 42–44]. Each coordination/conformation state can contribute to the peak. Thus, the peaks were deconvoluted and the values of the normalized area of each peak are plotted in Figures 5(a)–5(c). Interestingly, we observed two peaks around 739–742 cm^{-1}, interpreted as a free $TFSI^-$ peak. It was reported that the free $TFSI^-$ can show two different Raman peaks with different conformation states [44]. Thus, we assume that the two peaks are from free $TFSI^-$ with two conformation states. The peak area is correlated to the population ratio of the coordination state, assuming that the Raman signal intensity is equivalent for each state [33, 42]. An example of the deconvolution and the peak assignments is shown in Figures 5(d) and 5(e).

For $Mg(TFSI)_2$ in PCL-PTMC electrolytes, the free $TFSI^-$ peak area was the majority (ca. 0.8 fraction) at 8 wt.% $Mg(TFSI)_2$ and decreased to around a 0.6 fraction at 12–20 wt.% $Mg(TFSI)_2$. The free $TFSI^-$ peak area fraction again decreased to around 0.4 at 28–36 wt.% $Mg(TFSI)_2$. The bidentate peak area increased linearly from 16 wt.% to 36 wt.% $Mg(TFSI)_2$, where the "higher salt concentration" transition was observed in DSC. A significant monodentate peak fraction (ca. 0.4) was observed with 28 wt.% $Mg(TFSI)_2$, whereas there was more bidentate peak intensity with 36 wt.% $Mg(TFSI)_2$. In 36 wt.% $Mg(TFSI)_2$, the molar ratio of CL : TMC : Mg is 7.28 : 2.04 : 1 (Table 1). The ratio of C=O (CL+TMC) : Mg is around 9 : 1, which is the same EO : Mg ratio where the contact ion pair (CIP) was identified in PEO in a previous report [45]. Even though the coordination could be different in ester (in CL) and carbonate (TMC) from EO, this molar ratio can be related to the CIP formation.

For $Mg(TFSI)_2$ in PEO electrolytes, the peak area fraction associated with free $TFSI^-$ was around 0.9 at all salt concentrations, which indicates that the $Mg(TFSI)_2$ salt was mostly dissociated and existing as free (solvent-separated) ions. This is supported by the fact that all salt concentrations tested for PEO (highest at 36 wt.%, where EO : Mg = 24 : 1) are below the contact ion pair forming concentration (EO : Mg = 9 : 1) [45]. Thus, most Mg^{2+} was coordinated with EO rather than $TFSI^-$, unlike in the PCL-PTMC

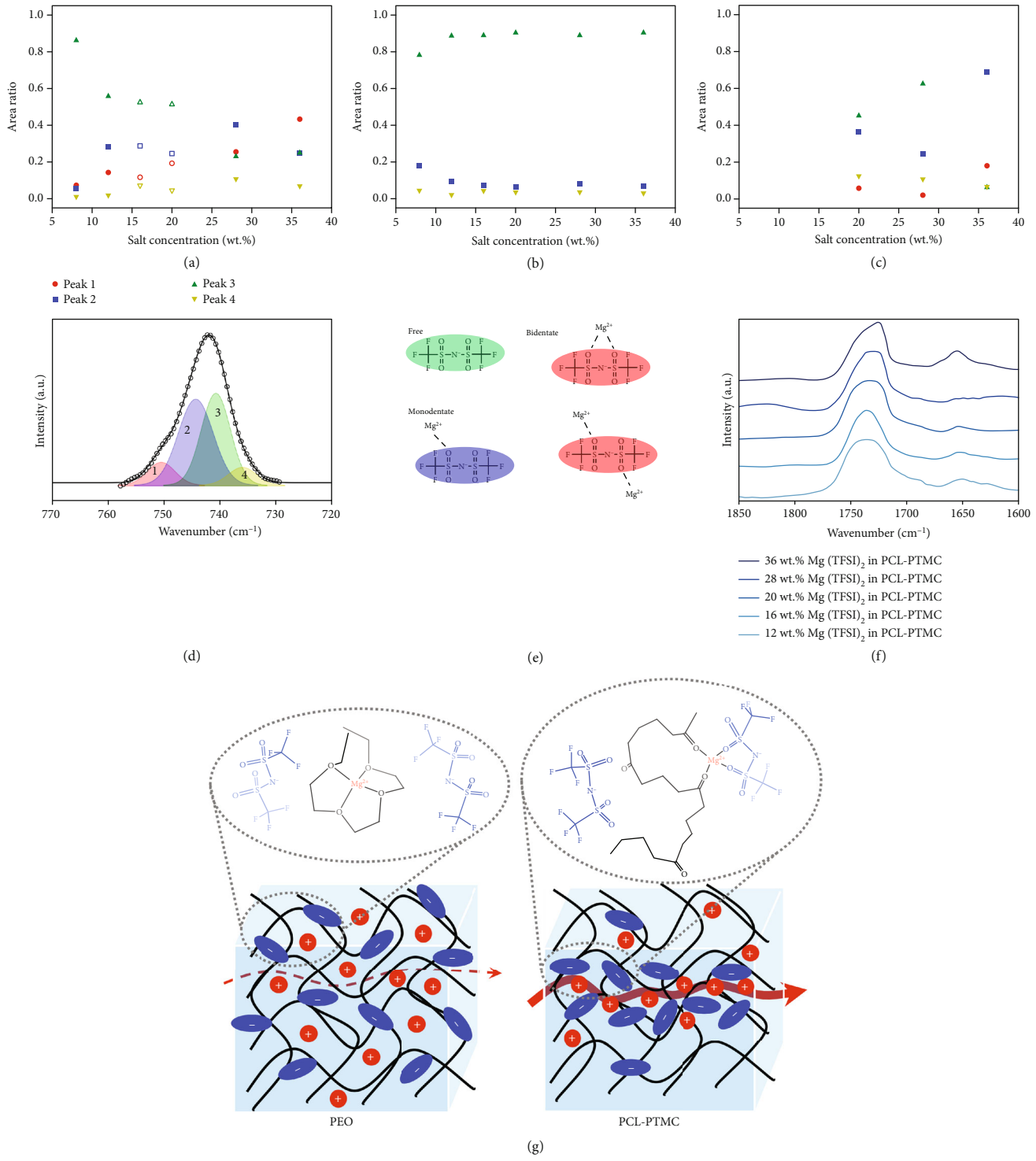

Figure 5: Peak area ratio of the deconvoluted $TFSI^-$ stretching peak of (a) $Mg(TFSI)_2$ in PCL-PTMC, (b) $MgTFSI_2$ in PEO, (c) LiTFSI in PCL-PTMC, (d) one example of Raman curve fitting and (e) the associated Raman peak assignments, (f) FT-IR of $Mg(TFSI)_2$ in PCL-PTMC, and (g) schematic representations of ion conduction and coordination in PEO and PCL-PTMC electrolytes.

electrolytes. This can be explained from the stronger coordination of Mg^{2+} to EO than C=O, as shown via the solution FT-IR experiments discussed in the previous section.

For comparison with the divalent magnesium PCL-PTMC electrolytes, Raman spectra of LiTFSI in PCL-PTMC, which exhibits high Li^+ transference number [25, 26], were also collected. For LiTFSI electrolytes, the peak shifts with the number of O on $TFSI^-$ coordinating with Li^+: $TFSI^-$ coordinating with more than 3 O (748-753 cm^{-1}, Peak 1), 2 O (745-748 cm^{-1}, Peak 2), 1 O (744-746 cm^{-1}, Peak 3), and free $TFSI^-$ (739-742 cm^{-1}, Peak 4) [46]. In LiTFSI in PCL-PTMC, the peaks were shifted to higher wavenumber than

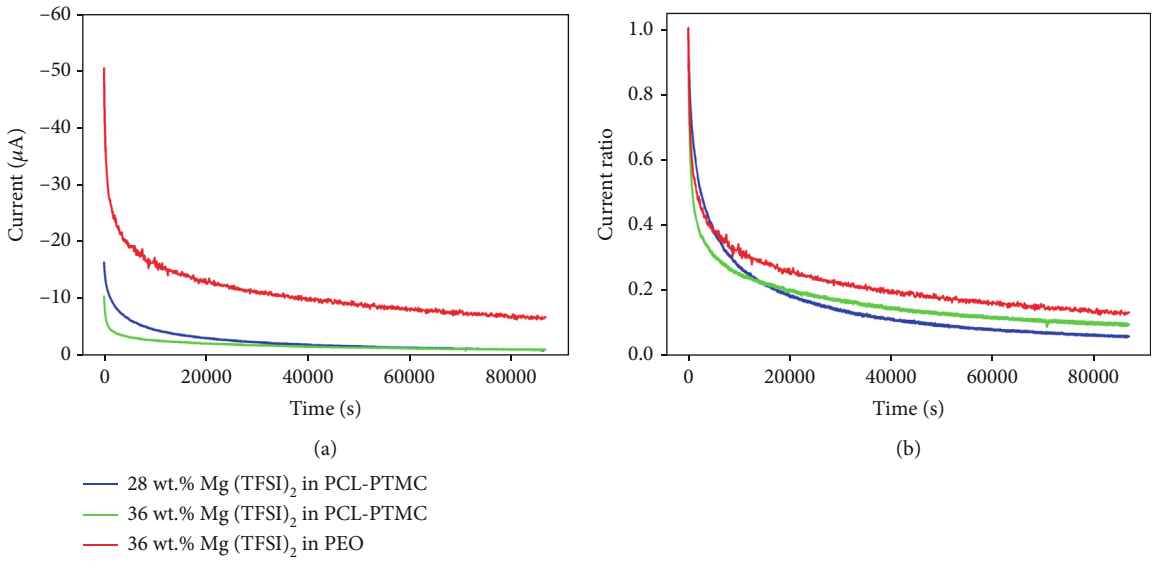

FIGURE 6: Polarization curves of Cu|Mg cells at -0.8 V vs. Mg/Mg^{2+}: (a) current (i) and (b) the current/initial current ratio (i/i_o) as a function of time (t).

$Mg(TFSI)_2$ in PCL-PTMC, which indicates higher number of O on $TFSI^-$ coordinating with Li^+. For the entire salt concentration range investigated the free $TFSI^-$ peak was low (~0.1). The Raman spectrum of 36 wt.% LiTFSI in PCL-PTMC indicated that most of $TFSI^-$ were coordinated with Li^+ on more than two O. This result supports the previously observed significant ion pair formation in LiTFSI in PCL-PTMC [25]. Also, the increased number of cations compared to $Mg(TFSI)_2$ resulted in more coordination with $TFSI^-$ anion. This is reasonable since the number of Li^+ is nearly twice the number of Mg^{2+} at the same wt.% salt. It can be concluded that higher cation transference numbers are possible when Raman spectroscopy indicates enhanced coordination of $TFSI^-$ with the cation, and here with the magnesium polymer electrolytes, the PCL-PTMC electrolytes support more $TFSI^-$ coordination than the PEO electrolytes (Figure 5(g)).

FT-IR spectra were obtained from $Mg(TFSI)_2$ in PCL-PTMC, as the vibration of the polar moieties in this polymer is sensitive to coordination (Figure 5(f)). The peak around 1730 cm^{-1} in the FT-IR spectra is related to C=O stretching: symmetric carbonyl stretching C=O in the carbonate of PTMC at 1735 cm^{-1} and in the ester of PCL at 1726 cm^{-1} [25]. It was reported that those stretching peaks shift to lower wavenumber when coordinated with cations, for example, a shift to 1700 cm^{-1} when coordinated with Li^+ [25] and 1720 cm^{-1} with Na^+ [24]. Assuming that the shift of the C=O stretching is proportional to the charge density of the coordinated cation, the shift of the stretching of the C=O coordinated with Mg^{2+} is estimated to be about 1659 cm^{-1} (Table S2). Thus, the peak around 1660 cm^{-1} can be related to the C=O coordinated with Mg^{2+}. Unlike the previously reported FT-IR spectra of LiTFSI in PCL-PTMC [25], the peaks cannot be deconvoluted to be analyzed in a quantitative manner due to (1) overlap of many peaks and (2) the limitation in the measurement condition (transmission mode on a substrate rather than ATR mode). Here, we instead compare the intensity of the peak to qualitatively analyze the population change. While the intensity of the stretching peak around 1660 cm^{-1} did not change with increased salt concentration up to 28 wt.%, the peak intensity was increased with 36 wt.% $Mg(TFSI)_2$. Thus, C=O participates more so in the coordination with Mg^{2+} above a threshold salt concentration. It is noted that these results mirror the calorimetry, ionic conductivity, and dielectric spectroscopy results as a function of salt concentration in PCL-PTMC, whereas at 36 wt.% $Mg(TFSI)_2$ there are significant differences from lower salt concentration electrolytes. We hypothesize that increased coordination of Mg^{2+} with the PCL-PTMC segments at 36 wt.% $Mg(TFSI)_2$ produces a slowing of chain relaxation that results in a significant reduction in ionic conductivity, despite the enhanced decoupling of ion conduction.

3.6. Polarization Test. To investigate the conduction and deposition of magnesium, polarization tests were performed on Cu|Mg cells at 80°C. Currents (i) and currents normalized by initial currents (i/i_o) were plotted as a function of time (Figure 6). The initial current (i_o), steady-state current (i_{ss}), and the steady-state current/initial current ratio (i_{ss}/i_o) obtained from the polarization tests are given in Table S3. The contribution of Mg^{2+} conduction out of the total ion conduction can be roughly estimated by the i_{ss}/i_o ratio for the Cu|Mg cells for the case of facile Mg metal electrodeposition/dissolution. It should be noted that this analysis cannot be used for quantitative conclusions regarding the Mg transference number here due to the interface issues described later. The i_{ss}/i_o ratio of 36 wt.% $Mg(TFSI)_2$ in PCL-PTMC in the Cu|Mg cell was about twice higher than that of 28 wt.% $Mg(TFSI)_2$ in PCL-PTMC. This difference might be due to the partially decoupled ion conduction mechanism and the increased coordination of C=O with Mg^{2+}. The i_{ss}/i_o ratio of 36 wt.%

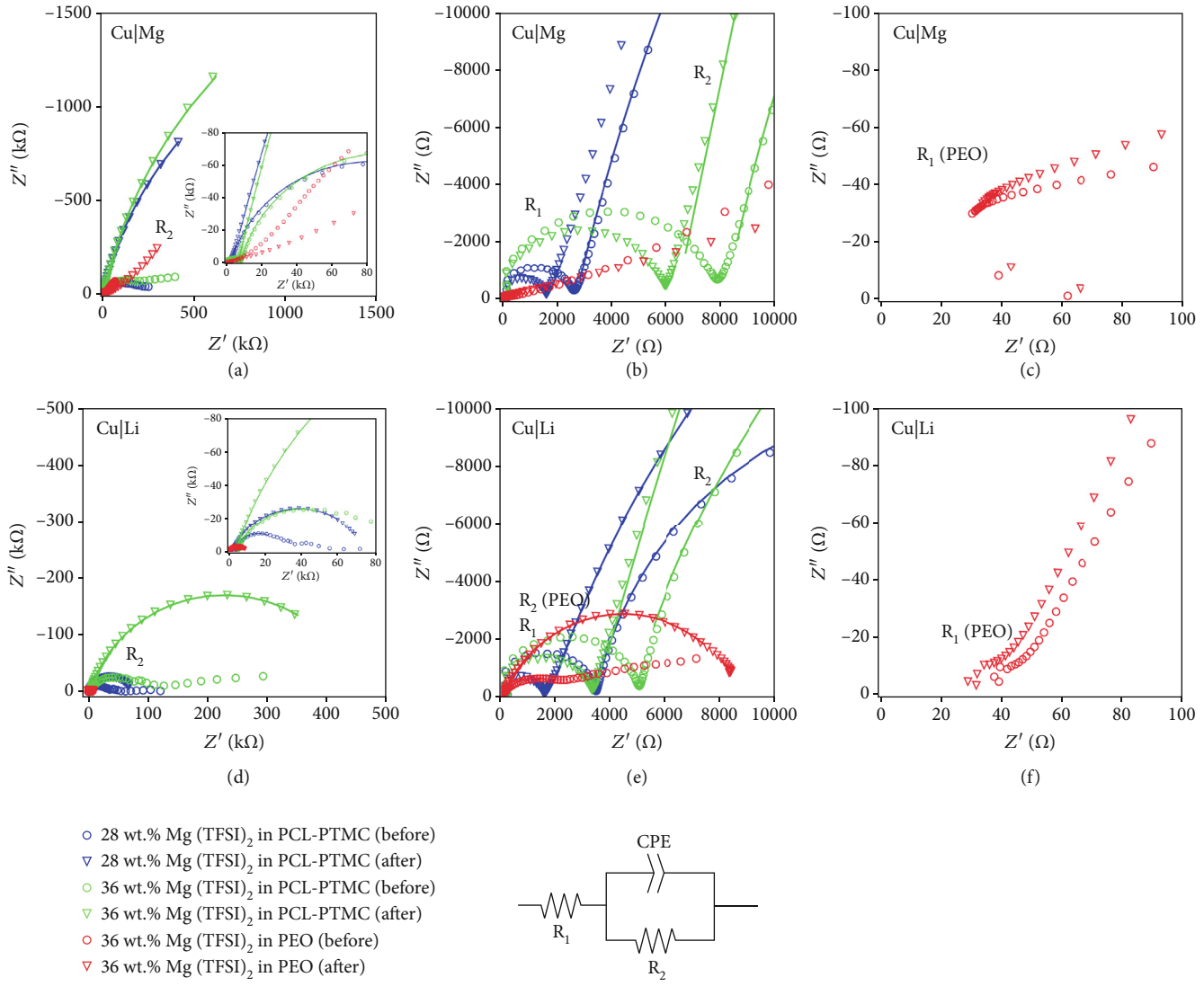

Figure 7: Impedance spectroscopy of (a–c) Cu|Mg cells, (d–f) Cu|Li cells. (a, d) Full scale, (b, e) magnified scale for the first semicircle for PCL-PTMC, and (c, f) magnified scale for the first semicircle for PEO. The circle and triangle markers indicate data points before and after polarization, respectively. The fitted curves are plotted as lines with the same color as the markers. In the equivalent circuit, R_1 was simplified as a resistor due to the convenience for fitting of R_2.

$Mg(TFSI)_2$ in PEO was close to that of 36 wt.% $Mg(TFSI)_2$ in PCL-PTMC.

Polarization tests on the magnesium polymer electrolytes were also performed on Cu|Li cells, which were used as a mechanism to circumvent the potential difficulties of stripping magnesium metal with the polymer electrolytes in the event of passivation of Mg by the $Mg(TFSI)_2$ (Figure S5). The initial current was lower for Cu|Mg cells than Cu|Li cells. This lower initial current with Cu|Mg cells implies the difficulty of Mg stripping.

3.7. EIS before/after Polarization. Impedance spectra were obtained before and after the polarization test on Cu|Mg cells and Cu|Li cells (Figure 7). The impedance spectra showed two semicircles, one in a smaller scale (R_1, $<10^4\Omega$) in the high-frequency range and one in a larger scale (R_2, $>10^5\Omega$) in the low-frequency range.

The resistance of the first semicircle (R_1) is related to the ionic conductivity, as can be determined via calculation (Table S4). The values of R_1 on Cu|Mg cells slightly decreased after polarization, which might be due to improved contact between the electrode and the polymer electrolyte or a decrease in thickness due to the compression. The decrease of R_1 is more significant (decreased by 1/2) and became smaller on Cu|Li cells than Cu|Mg cells, which indicates that the Mg^{2+} in the polymer electrolyte was exchanged with the Li^+ stripped from the Li metal counter electrode during the polarization.

The resistance of the second semicircle (R_2) is related to the charge transfer process and the interfacial resistance between the electrode and the polymer electrolyte (Figures 7(a) and 7(d)). For the cells containing PCL-PTMC polymer electrolytes before polarization, the impedance spectra showed a semicircle (R_2) followed by a rough

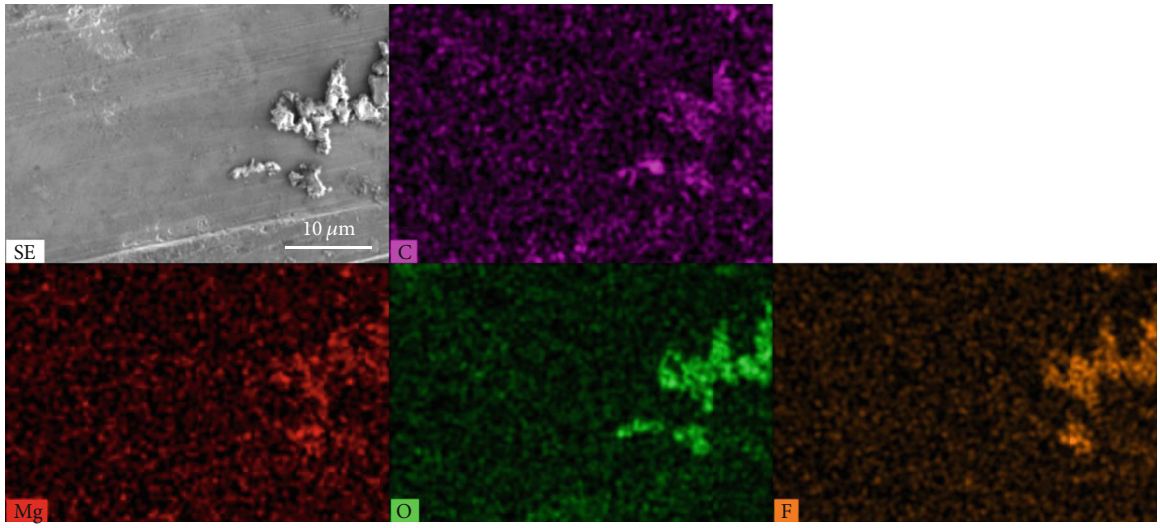

Figure 8: SEM-EDS image of Cu substrate after polarization of Cu|Mg cells containing 36 wt.% $Mg(TFSI)_2$ in PCL-PTMC.

horizontal line at low-frequency range, which might be due to the presence of multiple interfaces with different resistances (i.e., overlapping of multiple small semicircles in the impedance spectrum). The horizontal line disappeared after the polarization and merged to the large second semicircle. The formation of the large second semicircle indicates the buildup of decomposition species or the densified interface. The second semicircles were fitted to the equivalent circuit, and the R_2 values are shown in Table S5. Since the low-frequency impedance spectra of $Mg(TFSI)_2$ in PEO on Cu|Mg cells show a slope rather than a semicircle, those spectra were not fitted to the equivalent circuit. The slope was lower than a Warburg diffusion (i.e., 45° slope), which was observed under limited ion diffusion condition [47]. It might be related to the limited diffusion of the Mg^{2+} in PEO due to the strong interaction between Mg^{2+} and PEO. Also, the second semicircle of $Mg(TFSI)_2$ in PEO on Cu|Mg cells (in a very low frequency if possible) appears to be much larger than that of $Mg(TFSI)_2$ in PCL-PTMC in Cu|Mg cells. This indicates that the Mg deposition/stripping was not favorable with $Mg(TFSI)_2$ in PEO even with the higher ionic conductivity than $Mg(TFSI)_2$ in PCL-PTMC.

The values of R_2 of the Cu|Li cells were much smaller than those of the Cu|Mg cells, which indicates that (1) the Li deposition/stripping was much easier than that of the Mg and/or (2) the interface formed on Li counter electrode was more ion conductive than that on the Mg counter electrode. Unlike in Cu|Mg cells, the second semicircle of $Mg(TFSI)_2$ in PEO was much smaller than that of $Mg(TFSI)_2$ in PCL-PTMC in Cu|Li cells.

Figure S6 compares the impedance spectroscopy before the polarization on Cu|Mg and Cu|Li cells to investigate the resistance related to metal deposition/stripping process (i.e., the interfacial resistance, R_2). For all three investigated electrolytes, R_2 was larger on Cu|Mg cells than Cu|Li cells. In Cu|Li cells, the deposition/stripping process on the Cu electrode is Mg/Mg^{2+}, which is the same on Cu|Mg cells. The difference comes from the Li electrode, where the deposition/stripping process is Li/Li^+. Thus, the large R_2 on Mg|Cu cells was due to the Mg deposition/stripping on the Mg electrode.

3.8. Postmortem SEM-EDS Analysis. After the polarization tests, the copper electrode surface was analyzed by SEM-EDS.

The copper surface from the Cu|Mg cell was mostly clean with very sporadic particles, which were difficult to find. We analyzed the chemical composition of the particles on the copper electrode via EDS to determine if the particles were Mg deposits (Figure 8, Table S6). The deposits from the cell containing 36 wt.% $Mg(TFSI)_2$ in PCL-PTMC contained Mg, C, O, and F as shown in the EDS map. Atomic percentages of each element and the F/Mg ratio in the particle as determined via EDS are given in Table S6. Those numbers were compared to those of $Mg(TFSI)_2$ in PCL-PTMC polymer electrolytes. Firstly, the particle has 9 times higher Mg atomic ratio than 36 wt.% $Mg(TFSI)_2$ in PCL-PTMC electrolyte, indicating Mg deposition with a lot of decomposition products. Also, the F/Mg ratio of the particle was around 3 (i.e., $Mg^{2+} : TFSI^- = 2 : 1$), while the F/Mg ratio in $Mg(TFSI)_2$ is 12 and that of a $[MgTFSI]^+$ contact ion pair is 6. The TFSI ligand in the $[MgTFSI]^+$ contact ion pair is known to be labile to decomposition upon charge transfer [28]. The copper surface of the Cu|Li cells in $Mg(TFSI)_2$ in PCL-PTMC after polarization contained sharp Li-rich deposits (Figure S7) with higher Mg atomic ratio than the $Mg(TFSI)_2$ in PCL-PTMC polymer electrolyte (Table S7). This implies that the Mg^{2+} in the polymer electrolyte was exchanged with Li^+ from the Li electrode. In this case, Mg^{2+} might be conducted in either the Mg^{2+} or complex ($[MgTFSI]^+$ or others) form and deposited/decomposed on the Cu electrode.

4. Conclusions

Mg-conducting polymer electrolytes composed of $Mg(TFSI)_2$ in PCL-PTMC were investigated and compared to $Mg(TFSI)_2$ in PEO. Via calorimetry, it is observed that PCL-PTMC became amorphous with a small amount of magnesium salt (8 wt.%), while PEO had crystallinity within the studied salt concentration range (up to 36 wt.%), as observed previously with lithium salts. PCL-PTMC-based magnesium electrolytes show two types of glass transitions attributed to a lower salt concentration phase and a higher salt concentration phase, respectively. Both phases were observed in 16 and 20 wt.% $Mg(TFSI)_2$ in PCL-PTMC, and at higher salt loadings, only the higher salt concentration phase transition was observed. PCL-PTMC with 36 wt.% $Mg(TFSI)_2$ displays a lower total ionic conductivity than at lower salt loadings, even though the ion conduction appears to be partially decoupled from the polymer segmental relaxation. The interfacial resistance in Cu|Mg cells was much larger for $Mg(TFSI)_2$ in PEO electrolyte than $Mg(TFSI)_2$ in PCL-PTMC electrolyte, which might be due to the difficulty of Mg deposition/stripping and the interfacial resistance buildup between $Mg(TFSI)_2$ in PEO and the electrodes.

It is inferred from FT-IR and Raman spectroscopy that Mg^{2+} ions in high salt concentration PCL-PTMC electrolytes exist as ion complexes (Mg_xTFSI_y) rather than Mg^{2+} free ions. As previously reported with lithium salts, the interaction between the polar moieties of PCL-PTMC with Mg^{2+} was weaker than for PEO, which is expected to improve cation conduction. However, polarization of cells containing the magnesium PCL-PTMC electrolyte resulted in highly dispersed, F- and Mg-rich, particle-like deposits. A possible scenario is that the electrochemically more reducible $[MgTFSI]^+$ ion pairs were conducted and decomposed on the copper electrode to passivate the interface, inhibiting further deposition. It is expected that current generation salts that form ion pairs that are not reducible on the interface, such as carborane- or borate-based salts, may display better Mg deposition/stripping. Future use of an artificial solid electrolyte interphase to protect the Mg metal anode could also help to mitigate the electrodeposition/stripping issues. Furthermore, due to the interface issues, it was challenging to quantitatively compare the Mg^{2+} conductivity or cation transference number between the electrolytes. As future work, methods to overcome the interfacial issues and quantify the Mg conduction are being studied.

Data Availability

Main data are presented in the paper and the supplementary materials. The raw data used to support the findings of this study are available from the corresponding author upon request.

Conflicts of Interest

The authors declare no competing financial interest.

Authors' Contributions

Jennifer L. Schaefer and Jonas Mindemark conceived the project. Bumjun Park performed DSC, ionic conductivity, Raman spectroscopy, polarization test, EIS, and SEM-EDS. Bumjun Park, Sarah G. Pate, and Casey P. O'Brien performed FT-IR of solid polymer electrolytes. Bumjun Park and Jiacheng Liu performed dielectric spectroscopy analysis. Rassmus Andersson performed the FT-IR titrations of the polymer electrolytes, and the data was interpreted together with Guiomar Hernández and Jonas Mindemark. The work was supervised by Jennifer L. Schaefer.

Acknowledgments

We thank Prof. Ruilan Guo for DSC instrumentation and Tatyana Orlova and the University of Notre Dame Integrated Imaging Facilities for SEM. JM, GH, and RA acknowledge the financial support from STandUP for Energy. JLS, BP, and JL acknowledge the partial financial support from NSF CBET-1706370. JLS, BP, JL, CPO, and SGP acknowledge the additional financial support from the University of Notre Dame.

Supplementary Materials

Figure S1: differentiated heat flow curves of (a) PEO and (b) PCL-PTMC electrolytes. Figure S2: DSC cooling scans of 0–36 wt.% $Mg(TFSI)_2$ in PEO. Table S1: crystallinity and weight fraction of amorphous phase of $Mg(TFSI)_2$ in PEO. Figure S3: an example of the dielectric fitting. Figure S4: Raman spectra of $Mg(TFSI)_2$ in PCL-PTMC (a, b), LiTFSI in PCL-PTMC (c, d), and $Mg(TFSI)_2$ in PEO (e, f). Table S2: calculation of estimated shift of the C=O coordinated with Mg^{2+} using charge densities and the C=O shifts from Li^+ and Na^+. Figure S5: i vs. t curves of Cu|Mg (solid lines) and Cu|Li (dotted lines) with (a) 28 wt.% Mg(TFSI)2 in PCL-PTMC, (b) 36 wt.% $Mg(TFSI)_2$ in PCL-PTMC, and (c) 36 wt.% $Mg(TFSI)_2$ in PEO. Table S3: the initial current, steady-state current, and the ratio from the polarization tests on Cu|Mg cells. Table S4: estimated bulk resistance values calculated from the ionic conductivity using the cell dimensions. Table S5: R_2 values extracted from the EIS spectra by fitting with an equivalent circuit. Figure S6: impedance spectra before the polarization tests on Cu|Mg (circles) and Cu|Li (squares) cells with (a) 28 wt.% $Mg(TFSI)_2$ in PCL-PTMC, (b) 36 wt.% $Mg(TFSI)_2$ in PCL-PTMC, and (c) 36 wt.% $Mg(TFSI)_2$ in PEO. Table S6: atomic ratio (%) of Mg, C, O, and F from SEM-EDS on Cu electrodes from Cu|Mg cells after polarization. Figure S7: SEM-EDS elemental mapping from a Cu electrode from a Cu|Li cell with (a) 28 wt.% and (b) 36 wt.% $Mg(TFSI)_2$ in PCL-PTMC after polarization test. Table S7: atomic ratio (%) of Mg, C, and O from SEM-EDS on Cu electrodes from Cu|Li cells after polarization. *(Supplementary Materials)*

References

[1] T. D. Gregory, R. J. Hoffman, and R. C. Winterton, "Nonaqueous electrochemistry of magnesium: applications to energy

storage," *Journal of the Electrochemical Society*, vol. 137, pp. 775–780, 1990.

[2] D. Aurbach, Z. Lu, A. Schechter et al., "Prototype systems for rechargeable magnesium batteries," *Nature*, vol. 407, pp. 724–727, 2000.

[3] C. Liao, N. Sa, B. Key et al., "The unexpected discovery of the $Mg(HMDS)_2/MgCl_2$ complex as a magnesium electrolyte for rechargeable magnesium batteries," *Journal of Materials Chemistry A*, vol. 3, pp. 6082–6087, 2015.

[4] Z. Zhao-Karger, X. Zhao, O. Fuhr, and M. Fichtner, "Bisamide based non-nucleophilic electrolytes for rechargeable magnesium batteries," *RSC Advances*, vol. 3, pp. 16330–16335, 2013.

[5] L. C. Merrill and J. L. Schaefer, "Electrochemical properties and speciation in $Mg(HMDS)_2$-based electrolytes for magnesium batteries as a function of ethereal solvent type and temperature," *Langmuir*, vol. 33, pp. 9426–9433, 2017.

[6] S. Su, Z. Huang, Y. NuLi, F. Tuerxun, J. Yang, and J. Wang, "A novel rechargeable battery with a magnesium anode, a titanium dioxide cathode, and a magnesium borohydride/tetraglyme electrolyte," *Chemical Communications*, vol. 51, pp. 2641–2644, 2015.

[7] J. Muldoon, C. B. Bucur, A. G. Oliver et al., "Electrolyte roadblocks to a magnesium rechargeable battery," *Energy & Environmental Science*, vol. 5, pp. 5941–5950, 2012.

[8] Z. Zhao-Karger, M. E. Gil Bardaji, O. Fuhr, and M. Fichtner, "A new class of non-corrosive, highly efficient electrolytes for rechargeable magnesium batteries," *Journal of Materials Chemistry A*, vol. 5, pp. 10815–10820, 2017.

[9] J. Luo, Y. Bi, L. Zhang, X. Zhang, and T. L. Liu, "A stable, non-corrosive perfluorinated pinacolatoborate Mg electrolyte for rechargeable Mg batteries," *Angewandte Chemie, International Edition*, vol. 58, no. 21, pp. 6967–6971, 2019.

[10] O. Tutusaus, R. Mohtadi, T. S. Arthur, F. Mizuno, E. G. Nelson, and Y. V. Sevryugina, "An efficient halogen-free electrolyte for use in rechargeable magnesium batteries," *Angewandte Chemie, International Edition*, vol. 54, pp. 7900–7904, 2015.

[11] S. G. McArthur, L. Geng, J. Guo, and V. Lavallo, "Cation reduction and comproportionation as novel strategies to produce high voltage, halide free, carborane based electrolytes for rechargeable Mg batteries," *Inorganic Chemistry Frontiers*, vol. 2, pp. 1101–1104, 2015.

[12] B. Park and J. L. Schaefer, "Review—polymer electrolytes for magnesium batteries: forging away from analogs of lithium polymer electrolytes and towards the rechargeable magnesium metal polymer battery," *Journal of the Electrochemical Society*, vol. 167, article 070545, 2020.

[13] J. Mindemark, M. J. Lacey, T. Bowden, and D. Brandell, "Beyond PEO—alternative host materials for Li+-conducting solid polymer electrolytes," *Progress in Polymer Science*, vol. 81, pp. 114–143, 2018.

[14] Q. Zhang, K. Liu, F. Ding, and X. Liu, "Recent advances in solid polymer electrolytes for lithium batteries," *Nano Research*, vol. 10, pp. 4139–4174, 2017.

[15] B. Scrosati, F. Croce, and S. Panero, "Progress in lithium polymer battery R&D," *Journal of Power Sources*, vol. 100, pp. 93–100, 2001.

[16] L.-L. Yang, R. Huq, G. C. Farrington, and G. Chiodelli, "Preparation and properties of PEO complexes of divalent cation salts," *Solid State Ionics*, vol. 18–19, pp. 291–294, 1986.

[17] L. L. Yang, A. R. McGhie, and G. C. Farrington, "Ionic conductivity in complexes of poly (ethylene oxide) and $MgCl_2$," *Journal of the Electrochemical Society*, vol. 133, pp. 1380–1385, 1986.

[18] B. Park, H. O. Ford, L. C. Merrill, J. Liu, L. P. Murphy, and J. L. Schaefer, "Dual cation exchanged poly(ionic liquid)s as magnesium conducting electrolytes," *ACS Applied Polymer Materials*, vol. 1, pp. 2907–2913, 2019.

[19] D. Aurbach, Y. Gofer, A. Schechter et al., "A comparison between the electrochemical behavior of reversible magnesium and lithium electrodes," *Journal of Power Sources*, vol. 97–98, pp. 269–273, 2001.

[20] Z. Lu, A. Schechter, M. Moshkovich, and D. Aurbach, "On the electrochemical behavior of magnesium electrodes in polar aprotic electrolyte solutions," *Journal of Electroanalytical Chemistry*, vol. 466, pp. 203–217, 1999.

[21] N. Amir, Y. Vestfrid, O. Chusid, Y. Gofer, and D. Aurbach, "Progress in nonaqueous magnesium electrochemistry," *Journal of Power Sources*, vol. 174, pp. 1234–1240, 2007.

[22] R. Attias, M. Salama, B. Hirsch, Y. Goffer, and D. Aurbach, "Anode-electrolyte interfaces in secondary magnesium batteries," *Joule*, vol. 3, pp. 27–52, 2019.

[23] B. Sun, J. Mindemark, K. Edström, and D. Brandell, "Polycarbonate-based solid polymer electrolytes for Li-ion batteries," *Solid State Ionics*, vol. 262, pp. 738–742, 2014.

[24] C. Sångeland, R. Mogensen, D. Brandell, and J. Mindemark, "Stable cycling of sodium metal all-solid-state batteries with polycarbonate-based polymer electrolytes," *ACS Applied Polymer Materials*, vol. 1, pp. 825–832, 2019.

[25] B. Sun, J. Mindemark, E. V. Morozov et al., "Ion transport in polycarbonate based solid polymer electrolytes: experimental and computational investigations," *Physical Chemistry Chemical Physics*, vol. 18, pp. 9504–9513, 2016.

[26] M. P. Rosenwinkel, R. Andersson, J. Mindemark, and M. Schönhoff, "Coordination effects in polymer electrolytes: fast Li^+ transport by weak ion binding," *Journal of Physical Chemistry C*, vol. 124, pp. 23588–23596, 2020.

[27] J. Mindemark, B. Sun, E. Törmä, and D. Brandell, "High-performance solid polymer electrolytes for lithium batteries operational at ambient temperature," *Journal of Power Sources*, vol. 298, pp. 166–170, 2015.

[28] Y. Chen, N. R. Jaegers, H. Wang et al., "Role of solvent rearrangement on Mg^{2+} solvation structures in dimethoxyethane solutions using multimodal NMR analysis," *Journal of Physical Chemistry Letters*, vol. 11, pp. 6443–6449, 2020.

[29] N. N. Rajput, T. J. Seguin, B. M. Wood, X. Qu, and K. A. Persson, *Elucidating solvation structures for rational design of multivalent electrolytes—a review*, Springer International Publishing, 2018.

[30] R. Jay, A. W. Tomich, J. Zhang et al., "Comparative study of $Mg(CB_{11}H_{12})_2$ and $Mg(TFSI)_2$ at the magnesium/electrolyte interface," *ACS Applied Materials & Interfaces*, vol. 11, pp. 11414–11420, 2019.

[31] S.-B. Son, T. Gao, S. P. Harvey et al., "An artificial interphase enables reversible magnesium chemistry in carbonate electrolytes," *Nature Chemistry*, vol. 10, pp. 532–539, 2018.

[32] H. O. Ford, B. Park, J. Jiang, M. E. Seidler, and J. L. Schaefer, "Enhanced Li^+ conduction within single-ion conducting polymer gel electrolytes via reduced cation–polymer interaction," *ACS Materials Letters*, vol. 2, pp. 272–279, 2020.

[33] G. A. Giffin, A. Moretti, S. Jeong, and S. Passerini, "Complex nature of ionic coordination in magnesium ionic liquid-

based electrolytes: solvates with mobile Mg^{2+} cations," *Journal of Physical Chemistry C*, vol. 118, pp. 9966–9973, 2014.

[34] V. Bocharova and A. P. Sokolov, "Perspectives for polymer electrolytes: a view from fundamentals of ionic conductivity," *Macromolecules*, vol. 53, pp. 4141–4157, 2020.

[35] W. A. Henderson, F. McKenna, M. A. Khan, N. R. Brooks, V. G. Young, and R. Frech, "Glyme–lithium bis(trifluoromethanesulfonyl)imide and glyme–lithium bis(perfluoroethanesulfonyl)imide phase behavior and solvate structures," *Chemistry of Materials*, vol. 17, pp. 2284–2289, 2005.

[36] W. A. Henderson, "Glyme–lithium salt phase behavior," *The Journal of Physical Chemistry. B*, vol. 110, pp. 13177–13183, 2006.

[37] D. Brouillette, D. E. Irish, N. J. Taylor, G. Perron, M. Odziemkowski, and J. E. Desnoyers, "Stable solvates in solution of lithium bis(trifluoromethylsulfone)imide in glymes and other aprotic solvents: phase diagrams, crystallography and Raman spectroscopy," *Physical Chemistry Chemical Physics*, vol. 4, pp. 6063–6071, 2002.

[38] F. Kremer and A. Schönhals, *Broadband Dielectric Spectroscopy*, Springer Science \& Business Media, 2002.

[39] J. Liu, P. D. Pickett, B. Park, S. P. Upadhyay, S. V. Orski, and J. L. Schaefer, "Non-solvating, side-chain polymer electrolytes as lithium single-ion conductors: synthesis and ion transport characterization," *Polymer Chemistry*, vol. 11, pp. 461–471, 2020.

[40] D. R. MacFarlane, F. Zhou, and M. Forsyth, "Ion conductivity in amorphous polymer/salt mixtures," *Solid State Ionics*, vol. 113–115, pp. 193–197, 1998.

[41] C. Austen Angell, J. Fan, C. Liu, Q. Lu, E. Sanchez, and K. Xu, "Li-conducting ionic rubbers for lithium battery and other applications," *Solid State Ionics*, vol. 69, pp. 343–353, 1994.

[42] T. Watkins and D. A. Buttry, "Determination of Mg^{2+} speciation in a TFSI−-based ionic liquid with and without chelating ethers using Raman spectroscopy," *The Journal of Physical Chemistry. B*, vol. 119, pp. 7003–7014, 2015.

[43] S. Terada, T. Mandai, S. Suzuki et al., "Thermal and electrochemical stability of tetraglyme–magnesium bis(trifluoromethanesulfonyl)amide complex: electric field effect of divalent cation on solvate stability," *Journal of Physical Chemistry C*, vol. 120, pp. 1353–1365, 2016.

[44] M. Herstedt, M. Smirnov, P. Johansson et al., "Spectroscopic characterization of the conformational states of the bis(trifluoromethanesulfonyl)imide anion (TFSI−)," *Journal of Raman Specroscopy*, vol. 36, pp. 762–770, 2005.

[45] A. Bakker, S. Gejji, J. Lindgren, K. Hermansson, and M. M. Probst, "Contact ion pair formation and ether oxygen coordination in the polymer electrolytes $M[N(CF_3SO_2)_2]_2PEOn$ for M = Mg, Ca, Sr and Ba," *Polymer*, vol. 36, pp. 4371–4378, 1995.

[46] D. M. Seo, P. D. Boyle, R. D. Sommer, J. S. Daubert, O. Borodin, and W. A. Henderson, "Solvate structures and spectroscopic characterization of LiTFSI electrolytes," *The Journal of Physical Chemistry. B*, vol. 118, pp. 13601–13608, 2014.

[47] B.-A. Mei, O. Munteshari, J. Lau, B. Dunn, and L. Pilon, "Physical interpretations of Nyquist plots for EDLC electrodes and devices," *Journal of Physical Chemistry C*, vol. 122, pp. 194–206, 2018.